LETTERS
PUBLISHED ONLINE: 14 AUGUST 2017 | DOI: 10.1038/NNANO.2017.154
nature nanotechnology

All-electric control of donor nuclear spin qubits in silicon

Anthony J. Sigillito[1]*, Alexei M. Tyryshkin[1], Thomas Schenkel[2], Andrew A. Houck[1] and Stephen A. Lyon[1]

The electronic and nuclear spin degrees of freedom of donor impurities in silicon form ultra-coherent two-level systems[1,2] that are potentially useful for applications in quantum information[3] and are intrinsically compatible with industrial semiconductor processing. However, because of their smaller gyromagnetic ratios, nuclear spins are more difficult to manipulate than electron spins and are often considered too slow for quantum information processing. Moreover, although alternating current magnetic fields are the most natural choice to drive spin transitions and implement quantum gates, they are difficult to confine spatially to the level of a single donor, thus requiring alternative approaches. In recent years, schemes for all-electrical control of donor spin qubits have been proposed[4,5] but no experimental demonstrations have been reported yet. Here, we demonstrate a scalable all-electric method for controlling neutral ^{31}P and ^{75}As donor nuclear spins in silicon. Using coplanar photonic bandgap resonators, we drive Rabi oscillations on nuclear spins exclusively using electric fields by employing the donor-bound electron as a quantum transducer, much in the spirit of recent works with single-molecule magnets[6]. The electric field confinement leads to major advantages such as low power requirements, higher qubit densities and faster gate times. Additionally, this approach makes it possible to drive nuclear spin qubits either at their resonance frequency or at its first subharmonic, thus reducing device bandwidth requirements. Double quantum transitions[7] can be driven as well, providing easy access to the full computational manifold of our system and making it convenient to implement nuclear spin-based qudits using ^{75}As donors[8].

To demonstrate electrically driven nuclear magnetic resonance (EDNMR), an electron-nuclear double resonance technique (ENDOR) was used[9,10]. ENDOR requires both microwave and radiofrequency magnetic fields ($\mathbf{B}_1$ and $\mathbf{B}_2$, respectively) alongside radiofrequency electric fields ($\mathbf{E}_2$) to probe nuclei electrically. A high-quality-factor microwave resonator is needed to maintain a suitable signal-to-noise ratio. Although commercial ENDOR resonators exist, they require large powers and are incompatible with ultralow-temperature measurements. Moreover, they are designed to provide radiofrequency magnetic, but not electric, fields.

We circumvent these limitations by developing superconducting coplanar photonic bandgap resonators that allow broadband radiofrequency and microwave transmission above and below a lithographically defined photonic bandgap[11–13]. The bandgap is constructed by periodically alternating the impedance of a superconducting coplanar waveguide transmission line to form a one-dimensional microwave Bragg grating, as shown schematically in Fig. 1a. By incorporating a half-wavelength defect in the photonic bandgap, the device supports a resonant mode as shown in Fig. 1c, which can be used for electron spin resonance (ESR). Equivalently, this structure can be thought of as two discrete Bragg mirrors defining the boundaries of a half-wavelength cavity. The sample is located above

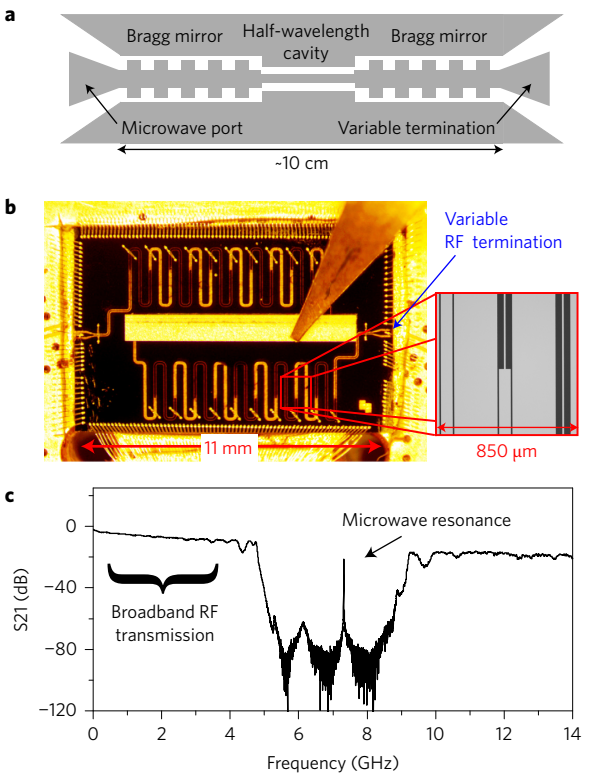

Figure 1 | Microwave photonic bandgap resonator design and performance. **a**, Cartoon schematic of a photonic bandgap resonator. The left port of the device is used for microwave excitation and readout, and the right port can be terminated to select whether radiofrequency (RF) electric or magnetic fields are present in the device. **b**, Optical micrograph of an actual device, with a silicon sample (bright rectangular feature) mounted using a phosphor bronze clip. The serpentine structures above and below the sample are the Bragg mirrors. Inset: zoomed-in view of an impedance step. **c**, Microwave transmission (S21) through the structure for the device in a magnetic field of 250 mT at a temperature of 1.9 K. The photonic bandgap spans the frequency range between 4.5 and 9 GHz with nearly lossless transmission below 4 GHz. The resonance appears at 7.3 GHz with a quality factor of 20,000. The loss outside the bandgap is due to the coaxial test cables, which were not calibrated out.

[1]Department of Electrical Engineering, Princeton University, Princeton, New Jersey 08544, USA. [2]Accelerator Technology and Applied Physics Division, Lawrence Berkeley National Laboratory, Berkeley, California 94720, USA. *e-mail: asigilli@princeton.edu

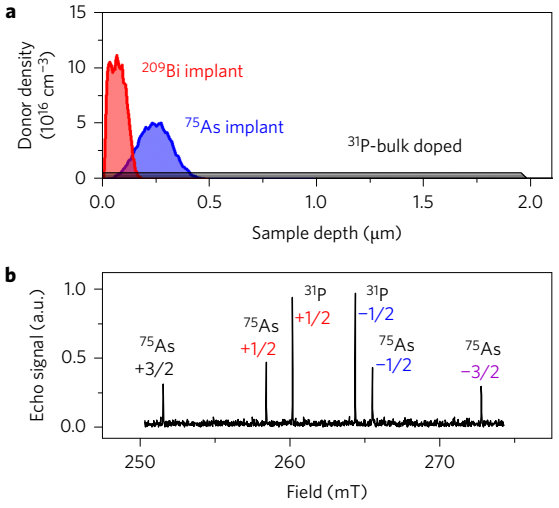

Figure 2 | ^{28}Si sample details. a, The sample consists of a ^{31}P-doped ^{28}Si epitaxial layer implanted with ^{209}Bi and ^{75}As. **b**, An echo detected field sweep spectrum, resolving the two ^{31}P and four ^{75}As hyperfine lines. The hyperfine lines are labelled by their nuclear spin projections with colours matching the data in Fig. 3. The data were taken at 1.9 K with a resonator frequency of 7.3 GHz.

the cavity region of the device. This resonator design has a continuous centre conductor that is isolated from the ground plane and allows for easy application of direct-current voltages or current biases, and it can be patterned directly on the silicon sample to offer enhanced sensitivity. To ensure that the spin signal only comes from the half-wavelength defect region of the resonator (and not spins within the Bragg mirrors), the sample was clipped to the surface of the resonator using a phosphor bronze spring (Fig. 1b). These devices require only one layer of lithography and will be convenient for other areas of quantum information processing and ESR. Considerations on the resonator fabrication and design are outlined in the Methods and in Supplementary Section 'Resonator simulation and design'.

The sample used throughout this work consists of a 2 μm isotopically enriched ^{28}Si epitaxial layer grown on a high-resistivity p-type substrate. The wafer has a (100) surface and, in this work, magnetic fields are always aligned in the plane of the surface along the (110) direction. The epilayer was grown to have 5×10^{15} ^{31}P cm^{-3}, and the sample was ion-implanted with ^{209}Bi and ^{75}As. After implantation, the donors were activated by annealing the sample in a N_2 atmosphere at 800 °C for 20 min (ref. 14). The simulated implantation profiles are shown in Fig. 2a (ref. 15). Two-pulse Hahn echo measurements were performed at 1.9 K, and an echo-detected field swept spectrum is shown in Fig. 2b, revealing the ^{31}P and ^{75}As hyperfine lines. Using pulsed spin counting techniques, we estimate the ^{209}Bi activation to be about 50% whereas the ^{75}As donors are fully activated. Because the ^{209}Bi signal is very weak (due to low donor activation and a large nuclear spin, 9/2), the ENDOR experiments were only performed on the ^{31}P and ^{75}As donors.

In the presence of $\mathbf{B}_1$ inhomogeneity, one can measure entirely different sub-ensembles of spins subject to different radiofrequency electric or magnetic fields by varying the microwave power[16]. It was therefore important to calibrate $\mathbf{B}_1$ before every ENDOR experiment by performing two-pulse Hahn echo experiments as a function of microwave power. The electric and magnetic field distributions are well known[17,18] and are plotted in Supplementary Fig. 2. It has been shown that inhomogeneity in $\mathbf{B}_1$ can be overcome by using adiabatic (BIR-WURST) pulses[16]. In Supplementary Fig. 3 we demonstrate that they also overcome $\mathbf{E}_2$ inhomogeneity. These pulse-shaping techniques make photonic bandgap resonators

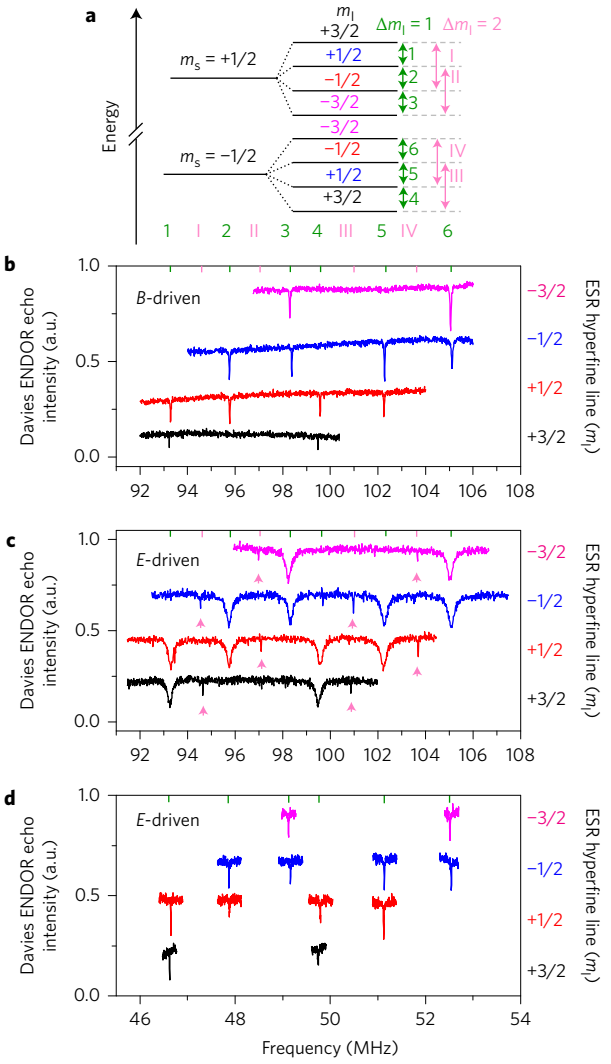

Figure 3 | NMR spectroscopy using either electric or magnetic fields. **a**, Energy level diagram illustrating the electronic Zeeman (m_S) and nuclear hyperfine (m_I) splittings for ^{75}As donors in Si. The $\Delta m_I = \pm 1$ and $\Delta m_I = \pm 2$ transitions are labelled using the green numbers and pink numerals, respectively. These labels are also used in **b**–**d**. **b**–**d**, Davies ENDOR spectra measured using magnetic (**b**) and electrical (**c**,**d**) RF pulses. The magnetically driven ENDOR spectra shows the six $\Delta m_I = \pm 1$ transitions, whereas the electrically driven spectra (**c**) reveal both the $\Delta m_I = \pm 1$ and $\Delta m_I = \pm 2$ transitions. Electrically driven ENDOR also resolves transitions at subharmonics of the $\Delta m_I = \pm 1$ transitions (**d**). The $\Delta m_I = \pm 1$ transitions in **b** are power broadened.

useful for complex ENDOR experiments requiring high-fidelity manipulations, but these advanced techniques were not necessary for the present work.

Davies ENDOR experiments were first performed using only radiofrequency magnetic ($\mathbf{B}_2$) fields (shorted device termination, see Methods). The ENDOR spectra for all four of the ^{75}As donor hyperfine lines are plotted in Fig. 3b, but the experiments were also performed on the ^{31}P donors (shown in Supplementary Fig. 4). Only the magnetic dipole allowed transitions could be resolved in this configuration. These are $\Delta m_s = 0$, $\Delta m_I = 1$, where m_s and m_I are the electronic and nuclear spin projections, respectively.

The device was reconfigured to have radiofrequency $\mathbf{E}_2$ fields in the sample (open termination, see Methods), and the measurements were repeated with the ^{75}As results presented in Fig. 3c (for ^{31}P data see Supplementary Fig. 4). In addition to the allowed ENDOR

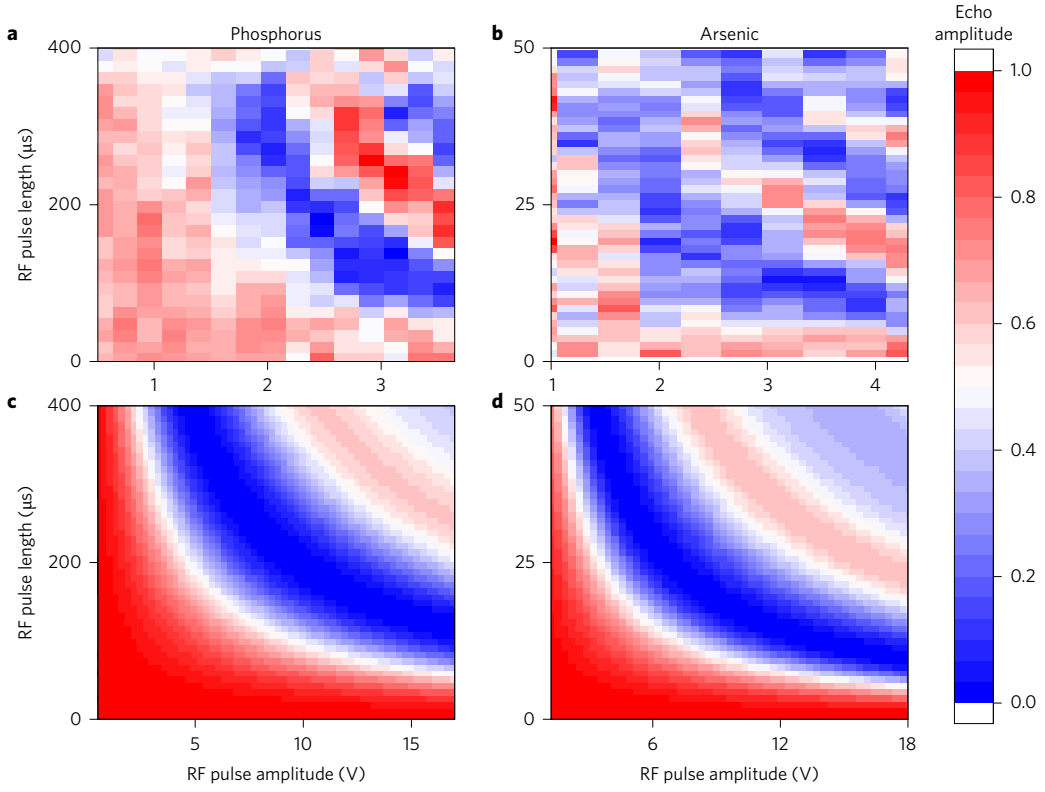

Figure 4 | Time-domain measurements of the ^{31}P and ^{75}As nuclear spins subject to an electrical drive. a,**b**, Rabi oscillations are recorded as a function of RF voltage amplitude for ^{31}P (**a**) and ^{75}As (**b**) subharmonic transitions. The ^{75}As transition is at 46.5 MHz and the ^{31}P transition is at 26.8 MHz. **c**,**d**, The simulated plots show similar dependences to the data, but larger RF amplitudes must be assumed, indicating that our models underestimate the Rabi frequencies by a factor of 3 to 4. The phosphorus simulation takes into account *g*-tensor modulation leading to an anisotropic hyperfine coupling, whereas the arsenic simulation also takes into account quadrupolar modulation. All data were taken at 1.9 K in a magnetic field of 250 mT.

transitions, several additional transitions appeared in the ^{75}As spectra (denoted by arrows in Fig. 3c). These very narrow transitions occur at exactly half the frequency of forbidden $\Delta m_I = 2$ transitions. The $\Delta m_I = 1$ transitions are power-broadened in this plot, because power was optimized for the $\Delta m_I = 2$ transitions. Transitions were also observed at subharmonics of the allowed transition frequencies and are shown in Fig. 3d.

The $\Delta m_I = 2$ transitions do not exist for ^{31}P donors because they have nuclear spin-1/2. EDNMR was observed at the fundamental and subharmonic transition frequencies for ^{31}P, but it was noticed that ^{31}P donors require more radiofrequency power than ^{75}As donors. To quantify the difference, two-dimensional EDNMR measurements of the Rabi nutation were conducted on both donors. These experiments used the standard Davies ENDOR pulse sequence but varied the radiofrequency pulse length and power. The data for the subharmonic transitions are plotted in Fig. 4a,b and the Rabi data for the fundamental transitions are shown in Supplementary Fig. 7. From these subharmonic data, it is clear that the arsenic donors respond over an order of magnitude more strongly to the electric fields (note the difference in the vertical axis scale), indicating that different mechanisms may be responsible for the EDNMR in these two donors. To verify that residual radio-frequency magnetic fields (due to the finite length of the device) cannot be responsible for the EDNMR, $\mathbf{B}_2$ was calibrated in the shorted device using a Rabi nutation experiment and the results were compared against the EDNMR data for both ^{31}P and ^{75}As. We found one would need 300 times more power for the residual $\mathbf{B}_2$ fields to account for the EDNMR.

We have identified two mechanisms that probably lead to the observed EDNMR, even though more theoretical and experimental work will be needed to confirm our explanation. To understand the EDNMR, we turn to the spin Hamiltonian common to group V donors in silicon. This is given by

$$H/h = \beta \mathbf{B}_0 \cdot \hat{g}_e \cdot \mathbf{S} + \mathbf{S} \cdot \hat{A} \cdot \mathbf{I} - \beta_n g_n \mathbf{B}_0 \cdot \mathbf{I} + \mathbf{I} \cdot \hat{Q} \cdot \mathbf{I} \qquad (1)$$

where β is the Bohr magneton, $\hat{g}_e$ is the electron gyromagnetic tensor, $\mathbf{S}$ is the electron spin, $\hat{A}$ is the hyperfine tensor, $\mathbf{I}$ is the nuclear spin, g_n is the nuclear g-factor, β_n is the nuclear magneton and $\hat{Q}$ is the nuclear quadrupole tensor. The terms in the spin Hamiltonian that are sensitive to electric fields are the electronic Zeeman ($\hat{g}_e$), hyperfine ($\hat{A}$) and quadrupolar ($\hat{Q}$) tensors. Because EDNMR is observed for both ^{75}As and ^{31}P (which has no quadrupole moment), we first neglect quadrupolar effects. Moreover, the ENDOR peak positions in Fig. 3 are well described assuming $\hat{A}$ is isotropic with coupling 198.25 MHz and $\hat{Q} = 0$.

Both $\hat{A}$ and g_e can be modulated through the hyperfine and spin–orbit Stark effects, respectively. These effects are quadratic to first order due to inversion symmetry at the donor site, but linear terms can arise from strain[19,20]. We therefore expect to drive transitions at both the electric field frequency, f and $f/2$ (because $\sin^2(f) \propto \cos(2f)$). Similar subharmonic transitions have been observed for electrically driven spin resonance in quantum dots[21,22]. Because the fundamental transition (at f) is strain-dependent, we will restrict our discussion to the subharmonic transition, which should be more robust against sample-specific strains.

Spin transitions cannot be driven solely by modulation of an isotropic hyperfine interaction due to the disparity in the electronic and nuclear precession frequencies. Any transition matrix elements involving A_{XX} and A_{YY} terms average out in the rotating wave approximation, and A_{ZZ} terms cannot drive spin rotations. We therefore require an anisotropic hyperfine interaction with A_{ZX}

terms to drive nuclear spins. To find the source of the anisotropy, we turn to the spin–orbit Stark shift.

We can compute the electric field modulation of g_e using multivalley effective mass theory[19] and experimentally measured Stark shift parameters[17,20], as outlined in Supplementary Section 'Estimation of Rabi frequencies for different physical mechanisms'. We find that the spin–orbit Stark shift directly modulates the quantization axis of the electron spin such that electron and nuclear spins are quantized along different axes. Radiofrequency electric fields then lead to non-zero A_{ZX} (as shown schematically in Supplementary Fig. 5), which can lead to nuclear spin rotations.

To test this mechanism against the experiment, we developed a model that simulates the Rabi nutation experiments in our device. This model accounts for rotation angle errors in both the ESR and NMR pulses, spin–resonator coupling, inhomogeneity in the radiofrequency and microwave fields and the implant profile of the donors. The simulation takes into account valley repopulation for electric fields in the (100) crystallographic directions (the dominant effect) but neglects the 'single valley' effect[19]. Therefore, these calculations probably underestimate the true Rabi frequency. Nevertheless, we find reasonable agreement with the experimental data for the phosphorus donors as shown in Fig. 4c. Note that the simulation is plotted on a different voltage scale, indicating a four-fold discrepancy between the simulation and data, which is reasonable given our necessarily rough estimates of the parameters. However, the equivalent ^{75}As simulation, taking into account only spin–orbit modulation of the electron spin quantization axis (shown in Supplementary Fig. 6), would require a 40 times larger radiofrequency voltage, which implies that another mechanism must dominate.

The only term in the ^{75}As Hamiltonian not present for ^{31}P is the quadrupolar coupling, so this is a possible source for the discrepancy in the EDNMR Rabi frequency data (Supplementary Fig. 6). It is difficult to determine transition frequencies for quadrupolar modulation, due to uncertainties in the screening potentials from inner shell electrons, and no studies have reported electric-field-induced modulation of the quadrupolar interaction. There have, however, been several recent reports of quadrupolar shifts for ^{75}As (refs 23,24) and ^{209}Bi donors (ref. 25) in silicon subject to strain. By comparing the reported strain-induced hyperfine splitting[24] to hyperfine Stark measurements[17], we can approximately scale the reported quadrupolar shifts[24] to correspond to the electric fields we apply in our experiments. By updating our model to including modulation of the quadrupolar interaction, Rabi frequencies are enhanced by a factor of more than 10, giving reasonable agreement with the experimental data, as shown in Fig. 4d. We therefore conclude that the quadrupolar interaction is most likely responsible for the spin transitions in ^{75}As; however, more theoretical work is warranted. We note here that while radiofrequency modulation of the quadrupole coupling is sufficient to produce fast Rabi nutations, it is too small to produce any noticeable shift or broadening in the ENDOR transitions.

For the largest radiofrequency electric fields applied in this work, the average Rabi frequency is ~70 kHz for the fundamental transition (Supplementary Fig. 7) and 60 kHz for its subharmonic. These applied fields are a factor of 10 below the donor ionization threshold, indicating that MHz-frequency EDNMR manipulations should be possible in unstrained Si. The fundamental transition Rabi frequencies depend on strain, suggesting that strain engineering should allow one to achieve even higher Rabi frequencies, and the ultimate limit is unknown.

These experiments probe two new physical mechanisms that manipulate donor nuclear spins in semiconductors. First, electric fields modulate the electron g-tensor to induce an effective anisotropic hyperfine interaction that appears to drive the ^{31}P nuclear spin transitions. Second, for ^{75}As, the quadrupolar interaction can be modulated to rotate nuclear spins. This mechanism relies not only on the electronic orbital structure, but also on the interaction of the inner shell electrons with the donor-bound electron. As such, this should lead to new physical insights into the donor electron system.

Our technique for controlling nuclear spins has several advantages over magnetic control. It relaxes the power requirements because voltages rather than currents are used, and allows for high-density, individually addressable arrays of donor nuclear spins, because electric fields are more easily confined than magnetic fields. By driving spins at subharmonics of their resonance frequencies and at subharmonics of double quantum $\Delta m_I = 2$ transitions, our electric field control method substantially reduces the bandwidth requirements for quantum devices while simultaneously providing easy acces to the expanded computational Hilbert space. From these results, one can envision new quantum computing architectures based on donor nuclear spins in silicon. These techniques should extend to other material systems with long coherence times such as donors in germanium[26], which offer a four-order-of-magnitude enhancement in the spin–orbit Stark shift[27,28]. The larger Stark effect should translate into significantly faster EDNMR gates.

Methods

Methods and any associated references are available in the online version of the paper.

Received 3 February 2017; accepted 3 July 2017;
published online 14 August 2017

References

1. Tyryshkin, A. M. *et al.* Electron spin coherence exceeding seconds in high-purity silicon. *Nat. Mater.* **11,** 143–147 (2012).
2. Morton, J. J. *et al.* Solid-state quantum memory using the ^{31}P nuclear spin. *Nature* **455,** 1085–1088 (2008).
3. Kane, B. E. A silicon-based nuclear spin quantum computer. *Nature* **393,** 133–137 (1998).
4. De, A., Pryor, C. E. & Flatté, M. E. Electric-field control of a hydrogenic donor's spin in a semiconductor. *Phys. Rev. Lett.* **102,** 017603 (2009).
5. Tosi, G. *et al.* Silicon quantum processor with robust long-distance qubit couplings. Preprint at http://arxiv.org/abs/1509.08538 (2015).
6. Thiele, S. *et al.* Electrically driven nuclear spin resonance in single-molecule magnets. *Science* **344,** 1135–1138 (2014).
7. Yusa, G., Muraki, K., Takashina, K., Hashimoto, K. & Hirayama, Y. Controlled multiple quantum coherences of nuclear spins in a nanometre-scale device. *Nature* **434,** 1001–1005 (2005).
8. Bartlett, S. D., de Guise, H. & Sanders, B. C. Quantum encodings in spin systems and harmonic oscillators. *Phys. Rev. A* **65,** 052316 (2002).
9. Davies, E. A new pulse ENDOR technique. *Phys. Lett. A* **47,** 1–2 (1974).
10. Tyryshkin, A. M., Morton, J. J. L., Ardavan, A. & Lyon, S. A. Davies electron–nuclear double resonance revisited: enhanced sensitivity and nuclear spin relaxation. *J. Chem. Phys.* **124,** 234508 (2006).
11. Yun, T.-Y. & Chang, K. One-dimensional photonic bandgap resonators and varactor tuned resonators. *Microwave Symposium Digest, 1999 IEEE MTT-S International* **4,** 1629–1632 (1999).
12. Liu, Y. & Houck, A. A. Quantum electrodynamics near a photonic bandgap. *Nat. Phys.* **13,** 48–52 (2017).
13. Bronn, N. T. *et al.* Broadband filters for abatement of spontaneous emission in circuit quantum electrodynamics. *Appl. Phys. Lett.* **107,** 172601 (2015).
14. Weis, C. D. *et al.* Electrical activation and electron spin resonance measurements of implanted bismuth in isotopically enriched silicon-28. *Appl. Phys. Lett.* **100,** 172104 (2012).
15. Ziegler, J. F., Ziegler, M. & Biersack, J. SRIM—the stopping and range of ions in matter (2010). *Nuclear Instrum. Methods Phys. Res. B* **268,** 1818–1823 (2010).
16. Sigillito, A. J. *et al.* Fast, low-power manipulation of spin ensembles in superconducting microresonators. *Appl. Phys. Lett.* **104,** 222407 (2014).
17. Sigillito, A. J., Tyryshkin, A. M. & Lyon, S. A. Anisotropic Stark effect and electric-field noise suppression for phosphorus donor qubits in silicon. *Phys. Rev. Lett.* **114,** 217601 (2015).
18. Malissa, H., Schuster, D. I., Tyryshkin, A. M., Houck, A. A. & Lyon, S. A. Superconducting coplanar waveguide resonators for low temperature pulsed electron spin resonance spectroscopy. *Rev. Sci. Instrum.* **84,** 025116 (2013).
19. Wilson, D. K. & Feher, G. Electron spin resonance experiments on donors in silicon. III. Investigation of excited states by the application of uniaxial stress and their importance in relaxation processes. *Phys. Rev.* **124,** 1068–1083 (1961).

20. Pica, G. *et al*. Hyperfine Stark effect of shallow donors in silicon. *Phys. Rev. B* **90,** 195204 (2014).
21. Laird, E. A. *et al*. A new mechanism of electric dipole spin resonance: hyperfine coupling in quantum dots. *Semicond. Sci. Technol.* **24,** 064004 (2009).
22. Romhányi, J., Burkard, G. & Pályi, A. Subharmonic transitions and Bloch–Siegert shift in electrically driven spin resonance. *Phys. Rev. B* **92,** 054422 (2015).
23. Franke, D. P. *et al*. Interaction of strain and nuclear spins in silicon: quadrupolar effects on ionized donors. *Phys. Rev. Lett.* **115,** 057601 (2015).
24. Franke, D. P., Pflüger, M. P. D., Mortemousque, P.-A., Itoh, K. M. & Brandt, M. S. Quadrupolar effects on nuclear spins of neutral arsenic donors in silicon. *Phys. Rev. B* **93,** 161303 (2016).
25. Pla, J. J. *et al*. Strain-induced nuclear quadrupole splittings in silicon devices. Preprint at http://arxiv.org/abs/1608.07346 (2016).
26. Sigillito, A. J. *et al*. Electron spin coherence of shallow donors in natural and isotopically enriched germanium. *Phys. Rev. Lett.* **115,** 247601 (2015).
27. Sigillito, A. J. *et al*. Large Stark tuning of donor electron spin qubits in germanium. *Phys. Rev. B* **94,** 125204 (2016).
28. Pica, G. & Lovett, B. W. Quantum gates with donors in germanium. *Phys. Rev. B* **94,** 205309 (2016).

Acknowledgements

The authors thank G. Pica, J.J.L. Morton and P. Bertet for insightful discussions. Work at Princeton was supported by the NSF through the Princeton MRSEC (grant no. DMR-01420541) and by the ARO (grant bo. W911NF-13-1-0179). Work at LBNL was performed under the auspices of the US Department of Energy under contract no. DE-AC02-05CH11231.

Author contributions

A.J.S., A.M.T. and S.A.L. conceived and designed the experiments. A.J.S. and A.A.H. designed the photonic bandgap resonators. T.S. supplied the samples. A.J.S. performed the experiments and modelling. A.J.S., A.M.T. and S.A.L. wrote the paper, with input from all authors.

Additional information

Supplementary information is available in the online version of the paper. Reprints and permissions information is available online at www.nature.com/reprints. Publisher's note: Springer Nature remains neutral with regard to jurisdictional claims in published maps and institutional affiliations. Correspondence and requests for materials should be addressed to A.J.S.

Competing financial interests

The authors declare no competing financial interests.

Methods

Resonator fabrication and design. The resonators used in this work were patterned in a 50-nm-thick Nb film electron-beam-evaporated on the surface of a C-plane sapphire wafer. The structures were defined using optical lithography and SF_6 plasma etching, as previously described[16,18]. The resonator has five periods of Bragg mirror on either side of the half-wavelength defect. Each period consists of both a high-impedance (95 Ω, 4 mm long) and a low-impedance (30 Ω, 4 mm long) strip of waveguide. The cavity is 6 mm long with a 10-μm-wide centre pin and 10 μm gaps. The simulated transmission spectra for this device geometry are provided in Supplementary Fig. 1. The radiofrequency termination is defined by either leaving the output port floating, or by shorting it to ground using Al wire bonds.

These resonators have a built-in feature that allows us to easily select whether electric or magnetic radiofrequency fields are present in the sample. The radiofrequency radiation used in this work has a wavelength that is large compared to the scale of the device and is unperturbed by the photonic bandgap, as it lies well below the gap. We can therefore set up radiofrequency standing waves by terminating the transmission line at the output port of the device (labelled 'variable termination' in Fig. 1a). A high-impedance (open) termination is used to enhance $\mathbf{E}_2$, whereas a low-impedance (shorted) termination enhances $\mathbf{B}_2$ in the sample. Due to the finite size of the device, one can never fully suppress the $\mathbf{E}_2$ and $\mathbf{B}_2$ fields, but we estimate that the residual undesired field amplitudes are reduced by at least a factor of 50 in the sample. $\mathbf{B}_1$ has a wavelength that is set by the $\lambda/2$ section of the device and is well confined by the two Bragg mirrors. It is unperturbed by the termination off chip, so we can select between $\mathbf{E}_2$ and $\mathbf{B}_2$ in the device without changing $\mathbf{B}_1$ or the ensemble of spins probed by the ESR.

The device was cooled to 1.9 K in a pumped helium cryostat equipped with a rotatable sample holder. This allows for *in situ* alignment of the device with an externally applied magnetic field $\mathbf{B}_0$ (ref. 18). With $B_0 = 250$ mT applied in the plane of the Nb, the microwave transmission spectrum (S21) was measured and is plotted in Fig. 1c. The photonic bandgap gives ~80 dB of attenuation from 4.5–9 GHz, and the microwave resonance appears at 7.3 GHz. The resonator is slightly undercoupled and has a temperature-limited quality factor of ~20,000. The spin sensitivity of this resonator was determined to be 5×10^6 spins per shot at 2 K using P-doped ^{28}Si (800 ppm ^{29}Si). This is on par with other planar resonators[16,18] and could be further improved by incorporating quantum-limited parametric amplifiers[29,30].

ENDOR measurements. We make use of the hyperfine interaction to read out the nuclear spin state (m_I) using the Davies ENDOR technique[9,10]. In this measurement, one probes the ESR transitions while simultaneously performing NMR. The ESR transition intensity depends on the nuclear spin state, so by performing conventional ESR on the donor electron spin one also obtains m_I. Before every experiment, the spins were prepared in thermal equilibrium using a combination of radiofrequency and optical pulses[10] because nuclear spin relaxation times are long at these temperatures.

To ensure that the subharmonic transitions were not artifacts driven by second harmonics generated in the radiofrequency source, the output of the radiofrequency source was fed directly into a spectrum analyser. We observed that, in the worst-case configuration, a second harmonic was present and attenuated by 35 dB compared to the fundamental harmonic. To further suppress this second harmonic, a set of seventh-order Butterworth low-pass filters (Crystek CLPFL) were used in every experiment, adding 35–50 dB of attenuation. Given the more than 70 dB power difference between the first and second harmonics, we can be confident that the observed subharmonic ENDOR transitions are not due to harmonics from the RF source.

Data availability. The data supporting the findings of this study are available within the paper and its Supplementary Information. The data are also available from the corresponding author upon reasonable request.

References

29. Eichler, C., Sigillito, A. J., Lyon, S. A. & Petta, J. R. Electron spin resonance at the level of 10^4 spins using low impedance superconducting resonators. *Phys. Rev. Lett.* **118,** 037701 (2017).
30. Bienfait, A. *et al.* Reaching the quantum limit of sensitivity in electron spin resonance. *Nat. Nanotech.* **11,** 253–257 (2016).